




# Investigating the seismic vulnerability of traditional ancient Tibetan buildings via structural subscaling experiments

Xiang Li<sup>1,2</sup> · Jiangan Sun<sup>1,3</sup> · Lei Xu<sup>1</sup> · Zhen Wang<sup>1</sup> · Lifu Cui<sup>1</sup> · Bin Liang<sup>4</sup> 

Received: 12 September 2023 / Accepted: 24 June 2024 / Published online: 16 July 2024  
© The Author(s), under exclusive licence to Springer Nature B.V. 2024

## Abstract

Traditional ancient Tibetan buildings (TATBs) date back hundreds of years. The seismic performance of TATBs constructed with stones and mud was analyzed by utilizing structural subscale features (materials, walls, and structures). The key to load-bearing in TATBs is the three-leaf stone wall. Based on the mechanical properties of materials, compression tests and quasistatic static tests of walls, this paper confirms that the seismic resistance capacity of the three-leaf stone wall of TATBs is unable to meet Chinese standards. The aims of this study are to present the dynamic behavior of TATBs by shaking table tests. According to the experimental data, the transcendence intensity magnification calculation method is modified to calculate the seismic vulnerability of TATBs. The results show that when the peak acceleration of ground motion is  $1.042 \text{ m/s}^2$ ,  $1.598 \text{ m/s}^2$  and  $2.881 \text{ m/s}^2$ , TATBs undergo slight damage, moderate damage, and severe damage, respectively.

**Keywords** Traditional ancient Tibetan structure · Three-leaf stone wall · Seismic vulnerability · Shaking table test · Quasistatic test

## 1 Introduction

Tibetan architecture is a precious traditional ancient architecture in China. The materials, shapes, layouts and construction techniques of traditional ancient Tibetan buildings (TATBs) are unique and have important inheritance value. The specificity of construction techniques and materials is expressed by the unique building wall texture and architectural style, which has become one of the most representative features of the Gyatong Tibetan region (Fig. 1) (Hu et al. 2009). Tibetan architecture is mainly distributed in the Aba Tibetan region, Qiang Autonomous Prefecture, Liangshan Yi Autonomous Prefecture and Ganzi Tibetan Autonomous Prefecture in Sichuan Province. The walls of TATBs represent

---

✉ Bin Liang  
Liang-Bin@mail.dlut.edu.cn

<sup>1</sup> College of Civil Engineering, Dalian Minzu University, Dalian, China

<sup>2</sup> College of Mechanical Science and Engineering, Northeast Petroleum University, Daqing, China

<sup>3</sup> School of Civil Engineering, Institute of Disaster Prevention, Beijing, China

<sup>4</sup> College of Civil Engineering, Dalian University of Technology, Dalian 116033, China

**Fig. 1** Traditional ancient Tibetan stone masonry structure



a three-leaf wall constructed with two leaf walls, and the space between the two leaf walls is filled with inferior materials (stones and/or bricks and mortar) (Silva et al. 2014, 2016). Currently, there is very limited quantitative information that can help to determine the vulnerability of TATBs. Therefore, it is necessary to study this type of architecture.

Assessing the vulnerability of TATBs to earthquakes is the top priority for preserving historic buildings. Based on seismic damage data (e.g., the 2008 Wenchuan 8.0 magnitude earthquake (Xu et al. 2009), 2012 Lushan 7.0 magnitude earthquake (Wang et al. 2021), and 2014 Kangding earthquake (Chen et al. 2017) of stone masonry structures, masonry structures have exhibited significant brittleness during past earthquakes (Rovero et al. 2016; D’Ayala et al. 2011; Carocci 2012; Lagomarsino et al. 2013). Earthquake damage in TATBs is mainly manifested in the collapse of load-bearing walls, the peeling of outer walls, and the cracking of the four corners of doors or windows (Fig. 2) (Xu et al. 2019; Jiang et al. 2022). Moreover, seismic performance assessments of TATBs are often hampered by a lack of information about materials and structural data. Moreover, antiseismic measures increase the heterogeneity of materials and structural data, which increases the lifetime of buildings (Yao et al. 2022; Liang et al. 2023a, 2023b).

As a historic construction material, stone has the advantages of low cost, easy availability and durability (Siegesmund et al. 2011; Hendry et al. 2001). The main overturning façade and vertical façade longitudinal response can be analyzed from a seismic damage perspective (D’Amato and Sulla 2021; de Carvalho Bello et al. 2020). The core dynamic properties of the trefoil wall and the sensitivity of the interstory interface can be further verified. Historic masonry monument preservation from the aspect of remote sensing technology or a seismic damage matrix (Fuentes et al. 2019) has been used to determine the characteristics of buildings with different levels of seismic damage (Gautam 2017; Brando



**Fig. 2** Damage to Tibetan buildings (Jiang et al. 2022)

et al. 2017a, 2017b; Chen et al. 2016; Boscato et al., 2018). This feature reflects the seismic performance of stone masonry structures, mainly in terms of mortar strength and block wall strength. There have been further developments in the study of the modulus of elasticity, shear discounting, and damage modes for mortar strength and block strength (Di Michele et al. 2023; D'Amato et al. 2023; Ravula and Subramaniam 2019; Kaushik et al. 2007). The dynamic behaviors of stiffness attenuation at the vertical level of a structure have also been the focus of researchers (Casolo and Milani 2013; Mazzon et al. 2010a, 2010b; Galetzka et al. 2015). Experimental research, mechanical model analysis and numerical simulation analysis of stone masonry buildings have shown that the mechanical properties of building materials are not always the same (Fuentes et al. 2019; Lagomarsino and Resemini 2009). The mechanical properties of building materials significantly impact the stiffness, deformation, stress–strain characteristics and bearing capacity of various wall and structural parameters (Krzan et al. 2015; Di Michele et al. 2023; Mazzon et al. 2010a, 2010b). Testing the mechanical properties of construction materials is the primary task for evaluating the seismic performance of TATBs.

In addition to the parametric characteristics of stone, mortar and infill materials, international scholars believe that it is necessary to study the mechanical behavior of stone walls (Zhao et al. 2022). Due to the lack of transverse connecting members, poor performance of mud mortar, and lack of detailed design of joints (Corradi et al. 2018; Borriet al. 2015), this type of masonry structure has the highest risk of in-plane or out-of-plane damage. Researchers have been devoted to the study of three-leaf stone walls: (a) Masonry wall-ettes were tested under static compression and/or diagonal compression to assess the basic mechanical properties of masonry in its as-built state. (Zhang et al. 2017; Li et al. 2023). (b) Three-leaf stone masonry walls under cyclic in-plane or out-of-plane action were tested in a limited number of experimental campaigns (Senaldi et al. 2013; Ferreira et al. 2015; Godio et al. 2019). (c) Although several building models made of two-leaf stone masonry were subjected to dynamic loading, the corresponding data on three-leaf stone masonry building models are still very limited. To better understand the seismic resistance of three-leaf stone walls in TATBs, Jiang et al. (2022) conducted an in-plane cyclic shear loading test. The failure mode, ductility, hysteresis behavior and energy consumption of three-leaf stone walls were investigated. Yang et al. (2020) analyzed the shear strength and failure mechanisms of three-leaf stone walls via double-shear tests. The study of the morphological and mechanical properties of three-leaf stone walls revealed that the mechanical properties, internal voids and geometric characteristics of materials strongly influence the compressive and shear strengths of stone masonry walls (Miccoli et al. 2017; Schiavi et al. 2019; Lombillo et al. 2013; Almeida et al. 2012). A shear strength test study of a three-leaf stone wall can detect the seismic performance of stone masonry. However, to study the seismic performance of stone masonry structures more accurately, shaking table tests are also needed.

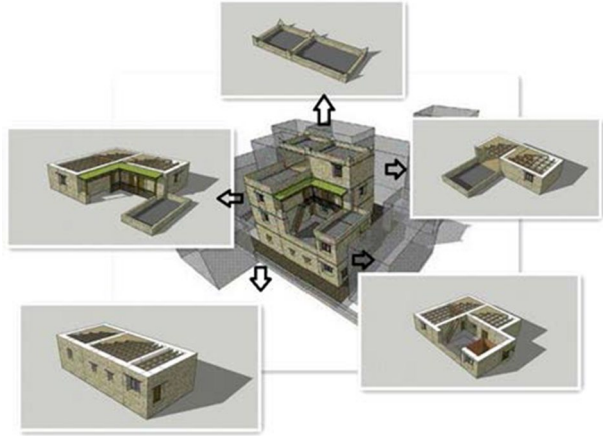
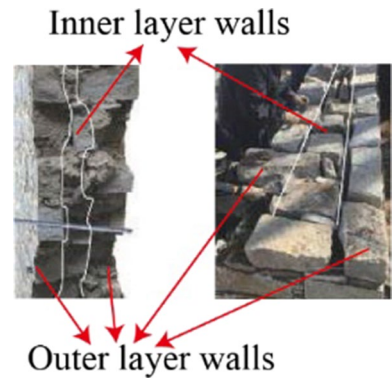
Experimental tests, mechanical model analyses and numerical simulations of stone masonry buildings have shown that various structural parameters have significant impacts on the stiffness, strength, deformation and bearing capacity. Ali et al. (2017, 2021) evaluated the seismic performance of traditional buildings by analyzing the damage state, acceleration, displacement response, and lateral force–deformation behaviors in shaking table tests of 1/3 and 1/4 scale traditional Dhajji Dewari building models. Xue et al. (2022) analyzed the vibration failure mechanisms of a 1:4 typical stone masonry structures by shaking table tests. Chavez and Meil (2013) analyzed the maximum substrate movement intensity of typical traditional stone temples that can still be repaired by shaking table tests. Costa et al. (Part 1 2013a; Part 2 2013b) tested the characteristics of the out-of-plane overturning

behavior of full-scale masonry by shaking table tests. Elmenshawi et al. (2014) evaluated the shear strength and intrinsic damping of stone masonry in the Western District of the Canadian Parliament District, Ottawa. Felice et al. (2022) contributed to the understanding of the seismic behavior of stone masonry by simulating the gradual loss of compactness of rubble masonry walls in a life-scale reproduction in shaking table tests until the two outer lobes separated and collapsed. Zhu et al. (2012) tested the dynamic behavior and seismic performance of the free vibration and tertiary seismic waves of a stone masonry structure by shaking table tests and verified that the stone masonry pagodas exceeded the limits specified in the Code for Seismic Design of Buildings (GB 50011–2010, 2010). Guerrini et al. (2019) evaluated the damage mechanisms, lateral displacement demand, hysteresis response and dynamic performance degradation of stone masonry structures under vibration. Mazzon et al. (2010) discussed the stiffness decay and structural failure mechanisms of multileaf stone walls in masonry structures. Giaretton et al. (2017) studied the principle of layered collapse of three-leaf walls by shaking table tests. Shaking table testing can help researchers better understand the seismic behaviors of historic stone masonry buildings. Rafi et al. (2019) identified four damage states of a typical two-story stone masonry building corresponding to structures at different seismic intensities by shaking table tests. Senaldi et al. (2019) studied the evolution of dynamic responses and damage mechanisms of stone masonry buildings via a unidirectional dynamic shaking table test. Vintzileou et al. (2015) conducted biaxial seismic tests on the seismic behaviors of historical clover masonry buildings. Therefore, it is necessary to study and evaluate the influence of physical parameters on the seismic response performance of TATBs during an earthquake.

To better understand the seismic behavior of TATBs, a shaking table test was conducted on a TATB at Yangzhai No. 194, Mudui Tibetan Township, Li County. Basic information about the structure of the TATB was obtained by onsite investigations. The experiments included material characterization tests, axial compressive tests and in-plane cyclic shear tests of masonry walls. A 1/5 scale model of the TATB was built for the shaking table test. The failure mode, dynamic characteristics, shear demand, seismic resistance, and seismic performance of the TATB were studied. According to the transcendence intensity magnification calculation method and the experimental results, the seismic performance of the TATB was quantitatively assessed.

## 2 Background and scope

TATBs represent valuable cultural heritage sites. Some typical representative buildings, such as the Potala Palace, Jokhang Temple, and Norbulingka Summer Palace, have been inscribed on the World Heritage List (2023). A field visit to Mudui Village, Ganbao Tibetan Township, Li County, Aba Tibetan and Qiang Autonomous Prefecture, Sichuan Province, was conducted to investigate the basic information of the TATB. Considering security, the window areas are relatively small. Most houses have 2 to 4 floors. The bottom floors are often used as a livestock enclosure. The top floors are mostly only half of the area of the partial buildings and are used for halls. The main building is made of stone and yellow mud. Wood is used for reinforcement and beams. The overall shape of the building is slightly upward (Fig. 3). The main load-bearing structure of the TATB is a trilobite wall. The TATBs are generally three-story with three-leaf stone walls (Fig. 4) with wide bottom widths and narrow upper widths. The thickness of the walls of the bottom floor is 600 mm. The thickness of the walls of the second floor is 500 mm. The thickness of the walls of the

**Fig. 3** Typical TATB**Fig. 4** Construction of the three-leaf wall of a TATB

third floor is 400 mm. The thickness of the walls of the roof parapet is 300 mm. The total height of the building is 9.34 m. The total weight of the building is approximately 479.3 tons. Wooden beams lap on top of the masonry walls, thereby transferring the upper loads.

### 3 Determination of the material properties of TATBs

The mechanical properties of the material need to be determined through testing. According to the requirements of Chinese building material testing standards, the material mechanical properties of stone and yellow mud were tested. The stone and yellow mud used in the experiment were obtained from established TATBs.

#### 3.1 Stone material

The stone used in TATBs is bluestone. The stone was drilled by a rhinestone for mechanical property testing (Fig. 5) (GB/T2542-2012, 2012). The stone specimen is shown in Fig. 6. Six specimens of stone were tested to determine their mechanical characteristics. The test was carried out under displacement-controlled loading. The mechanical characteristics of

**Fig. 5** Specimen design**Fig. 6** Specimens of stone**Table 1** Properties of the clay bricks

Type unit	Dimension/(mm) (D×H)	Density/(kg/m <sup>3</sup> )	Compressive strength/(MPa)
Stone block	43×150	2712.13 (0.007)	67.92 (0.077)

the stone are listed in Table 1 according to the relevant standard, with COV values given in parentheses. The stones selected for this study are similar to those found in the stone masonry structures of the region. The failure mode of the stone specimen was brittle failure (Fig. 7). The load displacement curve shows that the elastic stage was jagged (Fig. 8), which was caused by uneven density distribution and voids inside the stone.

### 3.2 Mortar

Mud is usually sifted before use in the standard construction procedure of mud mortar. However, workers usually omit this procedure to improve efficiency (Liang et al. 2023a, 2023b). Yellow soil is used as the main material in mud. Gradation analysis (GB 5009–2011 2011) (Figs. 9, 10) and mortar compressive strength tests (JGJ/T98-2010, 2010) were performed.

**Fig. 7** Crack distribution of the specimen



**Fig. 8** Compressive strength test force and displacement curve of the stone

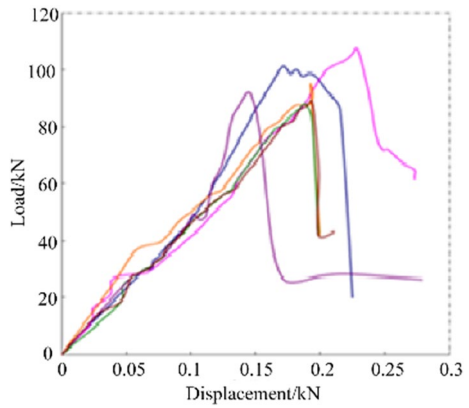


**Fig. 9** Shaking sieve



The soil grains in the yellow mud are mainly composed of sand. The sand grains are mainly medium sand grains and fine sand grains, which are mixed with some very fine sand grains, silt grains and breccia grains. The uniformity coefficient is  $C_u = \frac{d_{60}}{d_{10}} > 5$  ( $d_{60}$  is the defined particle size and  $d_{10}$  is the effective particle size). The yellow mud has good gradation (Table 2). The curvature coefficient is  $C_c = \frac{d_{30}^2}{d_{10} \cdot d_{60}}$  ( $d_{30}$  is the median

**Fig. 10** Yellow mud sieve allowance



**Table 2** Yellow mud gradation data

Sieve size/mm	Sieve allowance/kg	Sieve allowance ratio/%	Cumulative sieve allowance ratio/%	Cumulative sifting ratio/%
4.75	0.12	12	12	88
2.36	0.16	16	28	72
1.18	0.10	10	38	62
0.60	0.12	12	50	50
0.30	0.21	21	71	29
0.15	0.21	21	92	8
<0.09	0.08	8	100	0

**Fig. 11** The crack distribution of mud mortar

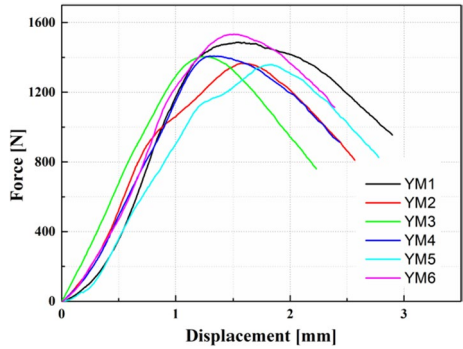


particle size). The lack of particles is mainly due to the presence of coarse sand particles in a range of 0.5–2 mm. Sand with large particle sizes has good permeability and is nonsticky. Yellow mud mortar mainly needs sand with relatively low permeability and is viscous when wet. According to the yellow mud gradation analysis test, the yellow mud basically met the test requirements.

The water content of the specimen was 23%. The specimens were cured for 30 days under outdoor conditions. The failure mode of the mud specimen was vertical layered peeling (Fig. 11). The density distribution inside the yellow mud was uniform, and the curve of the linear stage of the load displacement curve was relatively smooth (Fig. 12). The compressive strength of the cube of yellow mud mortar was 0.408 MPa. The



**Fig. 12** The load–displacement curve of mud mortar



standard deviation was 0.013. The coefficient of variation was 0.044. The arithmetic average of 1.3 times the measured value was used as the average value of the compressive strength of the specimen (JGJ/T70-2009, 2009).

## 4 The compressive strength test of masonry walls

### 4.1 Testing setup and procedures

According to GB/T50129–2011 (2011), the compressive strength of stone masonry walls was analyzed. The mechanical properties of the mortars and bricks are described in Sect. 2. The three-leaf walls (Fig. 13c, d) were 800 mm × 1200 mm × 400 mm in size (Fig. 13a, b). The high thickness ratio was  $\beta=4.17$ . The thickness of each layer of mud was strictly controlled within 15 mm. Each stone was soaked in water for 30 s before construction of the wall. The specimens were cured in the laboratory for 28 days at room temperature and maintained at 20 °C.

The compression test of stone masonry walls was carried out on a YAW-10000 J compression machine in the Structural Engineering Laboratory of Dalian Minzu University (Fig. 14). The compressive test of stone masonry was carried out according to the standard

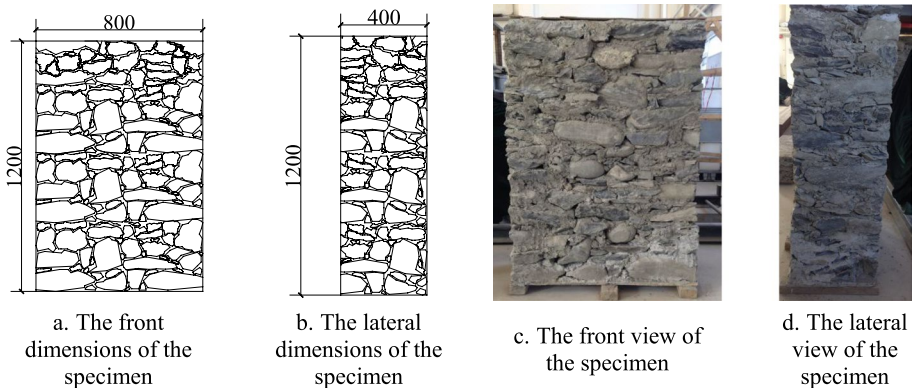


**Fig. 13** Specimen of Tibetan stone masonry

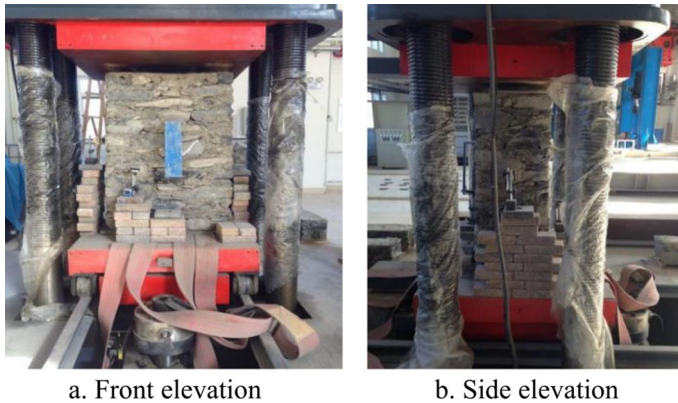


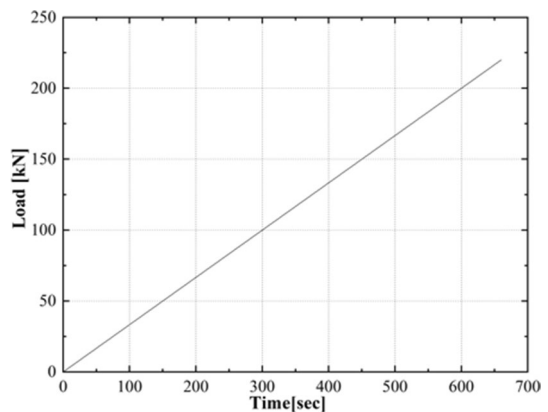
**Fig. 14** Layout of test setup

“Basic Mechanical Properties Test Method for Masonry” (GB/T50129–2011 2011). Displacement control was used to complete the loading process by step loading (loading control chart). Each step of the load was increased to 10% of the calculation failure load. In each step, the samples were evenly loaded within 1.0–1.5 min (Fig. 15). Each step was loaded evenly and continuously for a defined period of time, keeping the loading rate constant.

#### 4.2 Discussion of the results of the compressive strength test

The damage to the TATB walls showed irregular longitudinal penetrating cracks on the lateral sides (Fig. 16a) in the compression test. Multiple vertical cracks along the vertical mortar joints appeared on the front side (Fig. 16b). A large number of stones dropped off from the bottom of the wall (Fig. 16c). According to the load–displacement curve of the wall, the crushing process of the wall was divided into an elastic stage and a failure stage. Due to the uneven distribution of the mass and stiffness of the stone masonry wall, the load–displacement curve shows a sawtooth shape (Fig. 17). After the compressive strength of the stone masonry walls reached the elastic extreme, the wall maintained a period of ductility.

**Fig. 15** The axial pressure load displacement schedule



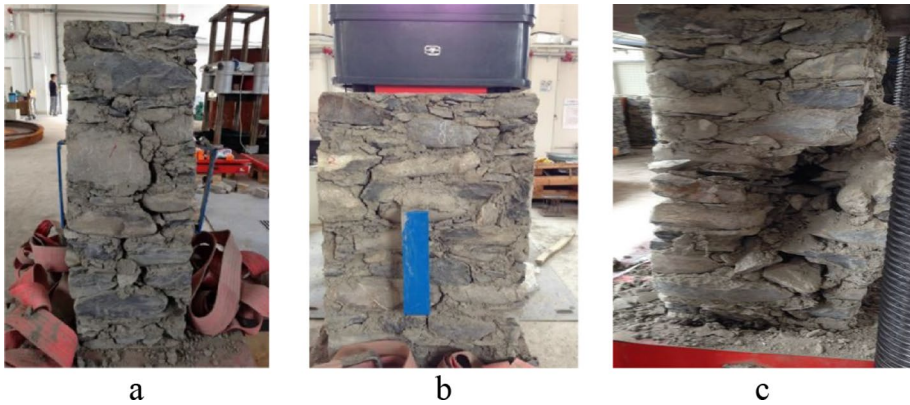
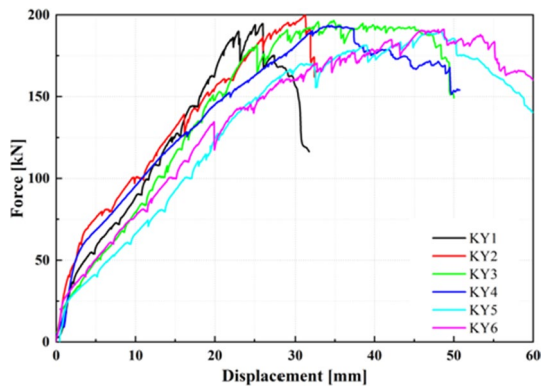


**Fig. 16** Typical damage distribution

**Fig. 17** Force–displacement relationships of the shear strength



According to the masonry design code (GB50003-2011, 2011), the masonry compressive strength design standard value can be calculated by the strength of the block and mortar (Eq. 1). The experimental and calculated values of compressive strength of Tibetan stone masonry are shown in Table 3.

$$f_m = f_1^\alpha (1 + 0.07f_2)k_1 \tag{1}$$

where  $k_1$  is the comprehensive coefficient of compressive strength of masonry ( $k_1$  is 0.01 from GB50003-2011);  $f_2$  is the compressive strength of mortar;  $f_1$  is the compressive strength of the unit; and  $\alpha$  is the influence coefficient of mortar.

## 5 Quasistatic test of the TATB

### 5.1 Specimen design

According to GB/T2542-2012 (2012), the wall size of the specimen is similar to that of a practical TATB wall with a ratio of 1:2.24. The thickness of the mud joints should be

**Table 3** Test results of Tibetan stone masonry compressive strength

No.	$P_{cr}/\text{kN}$	$P_u/\text{kN}$	$S_p/\text{mm}$	$\sigma/\text{MPa}$	$\bar{\sigma}/\text{MPa}$	Standard deviation	Variable coefficient	Calculated value of compressive strength
KY1	95.22	194.69	31.75	0.61	0.61	0.011	0.018	0.67
KY2	97.11	200.05	32.77	0.63				
KY3	96.45	196.54	49.99	0.61				
KY4	93.44	193.43	50.73	0.60				
KY5	85.98	189.83	59.91	0.59				
KY6	88.87	191.22	61.49	0.60				

$P_{cr}$ —Crack load;  $P_u$ —Peak load;  $S_p$ —Peak displacement;  $\sigma$ —Peak compressive strength;  $\bar{\sigma}$ —Mean peak compressive strength

reduced by reducing the geometric size ratio of the wall. However, if the thickness of the yellow mud mortar is reduced, it is bound to cause wall instability. The irregular alignment of the stone block makes it difficult to reduce the thickness of the mud in equal proportions. Therefore, the actual thickness of the yellow mud is 15 mm. Due to the irregularities of the stone masonry walls, a decrease in the size of the stone will affect the mechanical properties of the wall and change the contact relationship between the stone and the mud. Therefore, the specimen has the same sized stones as the actual wall.

The specimen was subjected to a cyclic shear loading test under axial compressive stress ( $\sigma_0=0.12$  MPa). The value of  $\sigma_0$  corresponds to the estimated vertical compressive stress of the wall, which considers the live load and weight of the structure. The structural dimensions and axial loads are shown in Table 4.

### 5.2 Testing apparatus specimen design

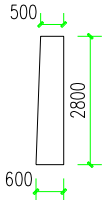
The specimens were cured for 6 months under natural ventilation. Then, the wall was moved to the test equation (Fig. 18). To better observe the cracks in the specimen, the side of the specimen was painted with burnt lime. The concrete beam under the wall was fixed to the solid ground by anchor bolts. The axial load was applied by a jack with a maximum load capacity of 2000 kN, which was transmitted to the wall by a steel beam. There were 5 rolling bars at the bottom of the steel beam that could be moved with the wall to avoid possible eccentricity caused by axial loads. The cyclic load was applied by a 1000 kN jack fixed to the reaction wall and transmitted to the wall by a steel beam.

Five displacement gauges, denoted  $U_i$  ( $i = 1, 2, \dots, 9$ ), were set up, as shown in Fig. 19, to measure the lateral displacement of the stone masonry wall and the displacement change of the concrete base.  $U_1$  measured the lateral displacement at the top of the wall.  $U_2$  measured the lateral displacement in the middle of the wall.  $U_3$  and  $U_4$  measured the displacement change in the concrete base to avoid the effect of the displacement change in the concrete based on the results of the experiment.

### 5.3 Loading system and test procedure

The axial load was applied to the top surface center of the beam by a vertical actuator, which remained constant during loading (JGJ/T 101-2015, 2015). The wall was preloaded laterally before the test. The preload value was 30% of the expected cracking load of the wall (Fig. 20a). The expected cracking load was calculated by Eq. 2 (GB

**Table 4** Design details of the wall specimen

No.	Prototype wall cross-section	Prototype wall specimen size	test wall specimen size	Axial load (kN)
First floor		4200 × 2800 × 500 (600)	1850 × 1250 × 220 (270)	55.27 kN

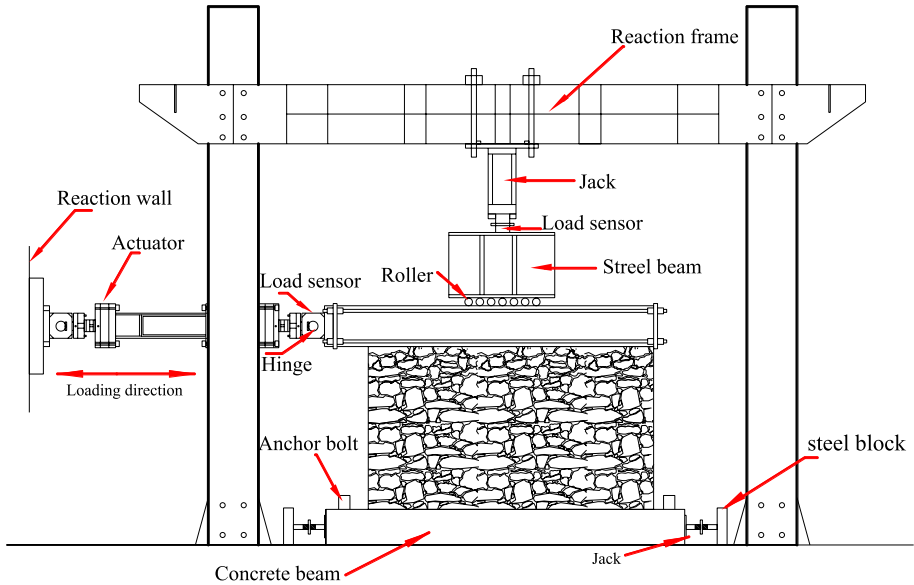
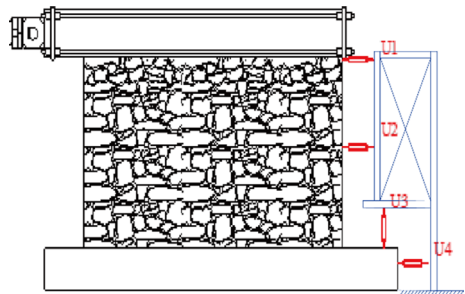


Fig. 18 Schematic view of the equipment

Fig. 19 Layout of the displacement gauges



50003–2011 2011). Combining the masonry block and mortar compressive strengths and the compressive strength of the wall, the value of the expected anticipated cracking load was calculated as 21.6 kN.

$$V = (f_{v0} + \alpha\mu\sigma_0)A_m \tag{2}$$

where  $A_m$  is the horizontal section area of the masonry wall,  $f_{v0}$  is the average shear strength of the masonry structure,  $\sigma_y$  is the vertical compressive stress of the masonry structure,  $\mu$  is the friction coefficient of the masonry, and  $\alpha$  is the shear-friction parameter.

The shear cyclic load was applied in increments of 5 kN at each stage (Fig. 20b) after ensuring proper operation of the sensor. Because the stone was soft and prone to brittle failure, the loading rate was kept stable at 0.025 kN/s. Three cycles were repeated at each step with the same loading to observe the degradation in the stiffness and strength. The loading mode with displacement as the control value was adopted before the wall yielded. The transverse cyclic force was increased by 16 kN per step after wall cracking.

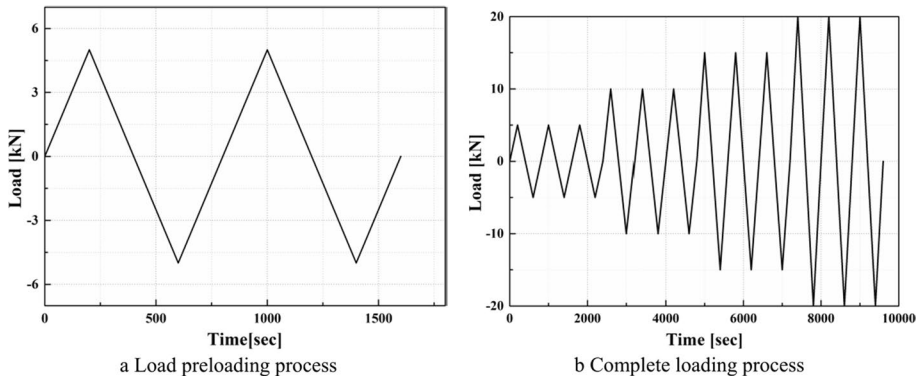


**Fig. 20** Lateral cyclic loading schedule

Two cycles were repeated at each step with the same loading. The test ended when the lateral load dropped to 85% of the lateral peak load.

#### 5.4 Discussion of the results of the Quasistatic test

The specimen was in the elastic phase of the wall during the preloading and the first and second loading phases. The first crack appeared in the lower right of the wall when the wall was loaded to 10 kN. Cracks gradually appeared on the wall, leading to the failure of the upper horizontal constraint with increasing horizontal load.

The plaster on the wall gradually fell off. Three millimeter-long cracks appeared on the wall. The cracks extended  $45^\circ$  to both sides of the wall. The mud joints of the wall gradually loosened (Fig. 21b). The wall entered the yield stage and gradually lost its bearing capacity. A large number of oblique cracks (Fig. 21a) and vertical cracks appeared on the wall when the load reached 22 kN. The wall plaster fell off in large quantities. A transverse crack appeared when the load reached 26 kN, which was formed under a horizontal shear load, and a small number of the vertical cracks were compression cracks. The widest crack was located in the middle of the wall with a width of 5 mm.

The hysteresis curve (Fig. 22) was spindle-shaped. The hysteresis curve area increased with the load level, and the hysteresis curve maintained a certain fullness, indicating an



(a) Oblique cracks



(b) The joints of the wall gradually loosened

**Fig. 21** Typical damage observations

**Fig. 22** Hysteresis loop for wall specimen

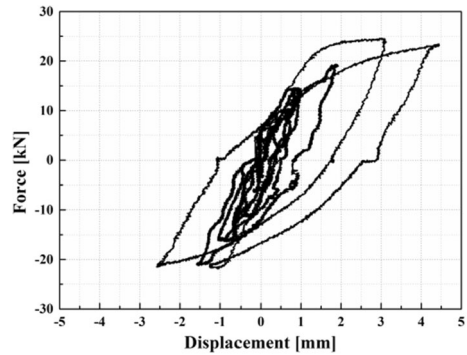
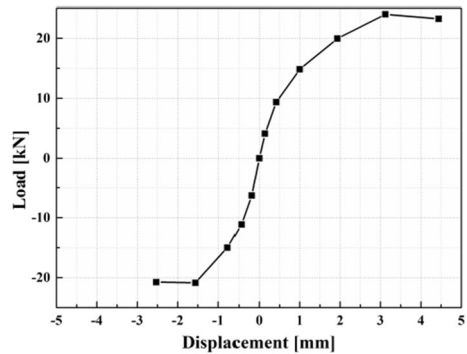


**Fig. 23** Skeleton curve

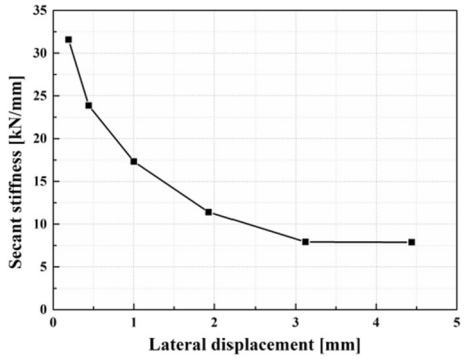


increase in the energy dissipation of the specimen. The number of cracks increased. The cracks gradually widened and expanded. Due to the sliding of the mud joints, X-shaped cracks appeared in the specimens with further increases in the transverse load. The hysteretic deformation gradually changed from a spindle shape to a bow shape.

According to the slope trend of the skeleton curve (Fig. 23), the damage to the specimen can be divided into three stages: the elastic stage, the hardening stage, and the destruction stage. The loads and displacements of these three stages were 11.2 kN and 0.48 mm, 26.5 kN and 3.23 mm and 23.2 kN and 4.48 mm, respectively. The specimen stiffness continued to decrease with increasing displacement (Fig. 24). In the elastic phase, the rate of degradation of the wall stiffness was significant. After entering the plastic phase, the decay rate of the specimen stiffness also decreased gradually. When the specimen was subjected to the ultimate load, the specimen stiffness reached the minimum value, 5.52 kN/mm, in the steady state. The ultimate bearing capacity and initial stiffness of the specimen were 26.5 and 32.3 kN/mm, respectively, which were lower than the limits of the local earthquake code (GB 50011–2010, 2010).



**Fig. 24** Stiffness degradation curve



## 6 Shaking table tests of the TATB

### 6.1 Model setup and instrumentation

A 1/5 scale model of a TATB was built (Candeias et al. 2017). The size of the model is shown in Fig. 26. The wall was made of mud and stone, and the thickness of the joint was 5 mm. The heights of the windows and doors were 300 mm and 2600 mm, respectively. The floor and roof were made of wood (e.g., the wooden beam section was 40 mm×50 mm, and the thickness of the wooden floor was 6 mm). The roof panel was made of 30 mm thick mud. The model was laid on a reinforced concrete slab base. The size of the reinforced concrete slab base was 3000 mm×2500 mm×200 mm. The concrete slab base was made of C25 concrete. The construction process is shown in Fig. 25. The specimen maintenance process was carried out indoors for 3 months. Plastic film was used for the intact model to ensure that the humidity and temperature of the maintenance environment corresponded to the area where the structure



a. Masonry walls in the bottom base



b. Beams and floor slab

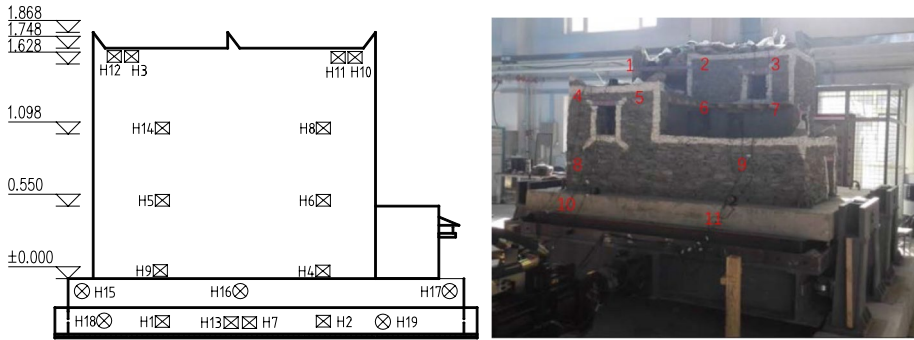


c. Masonry walls on the second floor



d. Completed model

**Fig. 25** Brief description of the construction process



a. schematic drawing of the sensor layout

b. actual image of the sensor layout

**Fig. 26** Detailed layout of the sensors

was located. During curing, the model was covered with plastic film to slow the evaporation of water.

## 6.2 Similitude design

Due to the limitations of the shaker size and load carrying capacity, scale models are widely used. The reduced-scale model can accurately reflect the real mode dynamic characteristics and failure modes. The similarity concept is utilized. There are three widely used methods for similarity (Dimitris et al. 2018), which ignore gravity, artificial mass simulation, and true replication. The artificial mass model changes the density of the structural model by adding counterweights so that the structural model satisfies the similarity requirement (Li et al. 2020). The gravity-ignoring model ignores the condition that the input acceleration similarity ratio is equal to the gravity acceleration similarity ratio in the similarity relationship, which in turn allows the structural model to satisfy the similarity requirement (wang et al. 2010). According to the importance of the effect of gravity on the dynamic behavior of TATBs, the artificial mass simulation method was adopted. The weight of the concrete slab base was 3.750 t. The total weight of the architectural model and the concrete slab base was 7.546 t.

Due to the limited load-bearing capacity of the shaking table, a model lacking artificial quality was used in the test. When the mass similarity ratio of the model was 1/60, the artificial counterweight was 4.2 t. The counterweight of each layer was as follows: the first layer was 2.0 t, the second layer was 1.4 t, and the third layer was 0.8 t. The total gravity load applied was 11.75 t. Due to the lack of artificial quality models, the vertical stress similarity ratio caused by gravity was  $S_\sigma = 1/2.4$ . Considering that the model was mainly subjected to horizontal shear forces, the design shear stress similarity ratio  $S_\tau = 1$ . The shear strain similarity constant was equal to 1. The similarity ratios of the other parameters are shown in Table 5.

## 6.3 Input excitation and testing protocols

The size of the shaking table is 3.00 m × 3.00 m. The parameters of the shaking table are shown in Table 6. The displacement sensor has a range of 100 mm. The frequency range of the shaking table is 0–80 Hz. The maximum acceleration measurement range of the

acceleration sensors is 3 g. The frequency range of the acceleration sensors is 0–500 Hz. The sensitivity of the acceleration sensors is 1%. Twenty displacement sensors and acceleration sensors were installed on the structural model (Fig. 26a). These sensors were installed at locations where the highest response expected could be obtained. The layout of the sensors is shown in Fig. 26.

The El Centro earthquake wave was chosen as the input earthquake excitation in this study. The acceleration time history and displacement time history are shown in Fig. 27. The record was scaled in the time domain for the shaking table test. The peak displacements were 8.34, 12.18 and 15.89 mm, respectively. The corresponding peak accelerations were 1.042, 1.598 and 2.881  $\text{m/s}^2$ , respectively.

### 6.4 Damage observed and analysis of the results

#### 6.4.1 Observed damage

The oblique shear cracks appeared at the vertical and horizontal corners of the wall when the peak acceleration of ground motion was 1.042  $\text{m/s}^2$ . The cracks developed obliquely along the walls at the end of the beam top of the door and window. Some cracks extended

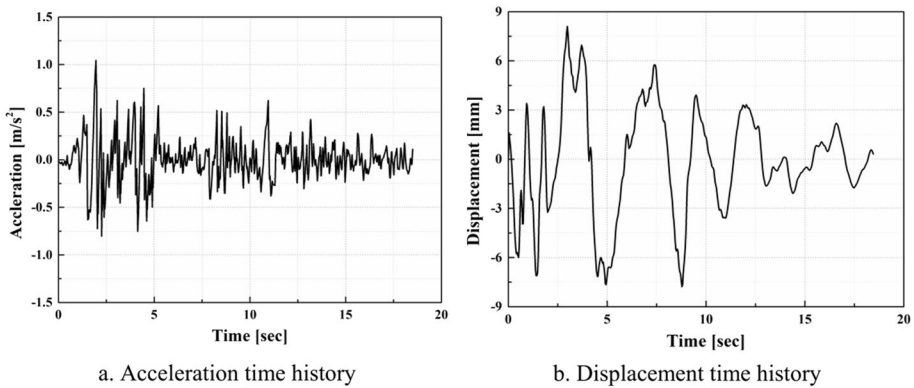


Fig. 27 El centro wave

Table 5 Similitude scaling factors

Physical quantity	Similitude scale factor	Physical quantity	Similitude scale factor
Displacement	$S_l = 1/5$	Stiffness	$S_k = 1/5$
Modulus	$S_E = 1$	Acceleration	$S_a = 2.4$
Time	$S_t = 1/3.5$	Damping	$S_c = 1/17$
Mass	$S_m = 1/60$	Poisson's ratio	$S_\nu = 1$

Table 6 Performance parameters of the ground shaking table

Table dimension/m	Maximum displacement/mm	Maximum payload/t	Frequency range/Hz
3.00 m × 3.00 m	± 80	50	0.1–50

**Fig. 28** Distribution of wall cracks between axis B–C



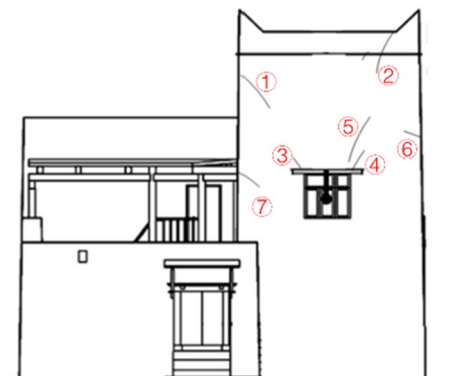
to the junction of the longitudinal and transverse walls. A horizontal crack appeared at the windows on the second floor when the peak acceleration of ground motion was  $1.598 \text{ m/s}^2$ . The original crack extended upward across the entire wall. Oblique cracks along the cracks appeared at the corners of the wall with doors and windows in the B and C axes. When the peak acceleration of ground motion was  $2.881 \text{ m/s}^2$ , the crack expansion caused the roof to separate from the wall. The wall was extensively damaged. The stones were delaminated and fell from the walls, which led to wall collapse at the corner. The cracking of the specimens was mainly concentrated in the corners of the third floor and the window positions of the second floor (Fig. 28).

Due to the large, concentrated stress at the windows and doors of the specimen and the gradual decrease in the wall thickness of the specimen, the bearing capacity and stiffness changed suddenly at the four corners of the window on the second floor, leading to oblique cracks on the wall. These diagonal cracks first arose at the corners of the top floor, followed by the upper corners of the windows, and then extended toward the transverse walls. The sequence in which the diagonal cracks were generated is shown in Fig. 29. In addition, the weak tensile strength of the longitudinal and horizontal walls and the weak strength of the mud were also reasons for wall cracking. The damage state of the specimen was similar to the seismic damage state of the stone masonry structure in the introduction section.

#### 6.4.2 Acceleration response of the TATB

For the irregular façade characteristics of the TATB, the structural response accelerations of floors 2 and 3 under different seismic excitations are discussed. Based on the

**Fig. 29** Schematic diagram of the crack distribution



acceleration time histories at each measurement point, the peak accelerations of the specimens can be derived at peak displacement waves of 8.34, 12.18 and 15.89 mm. The peak accelerations at the second and third floors are shown in Table 7. The variation in the peak along the height direction is shown in Fig. 30. The corresponding acceleration amplification factors are shown in Fig. 31. The acceleration of the superstructure increased as the peak surface displacement increased. Moreover, the peak acceleration of the same floor differed by approximately 10%, which was mainly caused by the torsional effect of structural asymmetry. Figures 30 and 31 show that along the height of the building, the floor acceleration increased gradually, especially in Case No. 3. The increase in acceleration was more pronounced on the third floor, which was due to the change in mass and stiffness of the building along the vertical direction.

### 6.4.3 Interlayer displacement of the TATB

The displacement response of the TATB increased with increasing acceleration of ground motion (Fig. 32). The displacement response of the third floor of the TATB was the largest (Table 8), indicating that the horizontal wall shaking in this part was more obvious. When the peak acceleration of the ground motion was  $2.881 \text{ m/s}^2$ , the displacement of the wall at the third floor was too large, resulting in a large number of cracks. Moreover, the interlayer displacement response of the structure was the largest at that time. The peak displacement of the same floor differed by approximately 10%, indicating that the structure had asymmetric torsion. According to the interlayer displacement (Fig. 32), the displacements of the second and third floors were significantly larger than that of the first floor, which indicates that the mass and stiffness of the specimen suddenly changed in the vertical direction. There was a weak layer between the first floor and second floor. Moreover, only two low walls with low plane stiffness in the direction of earthquake action were easily damaged.

## 7 Assessment of the seismic resistance of the TATB by the transcendence intensity magnification calculation method

Based on the mechanical characteristics of the construction materials of the TATB, the compressive and shear strengths of masonry walls, and the experimental shaking table test data, this chapter predicts the failure state of structures under different seismic action intensities. The seismic resistance of the TATB was evaluated from the perspective of the excess strength ratio. The calculation methods of seismic shear conversion acceleration and yield acceleration are suitable for multilayer masonry structures. According to the research ideas in Chinese specifications (JGJ161-2008, 2008) and references (Yin and Yang 2004; Liu and Sun 2014), a calculation method for the transcendence intensity ratio that is more suitable for masonry is proposed. The ratio of seismic shear to resistance is taken from the excess strength rate of single-layer masonry structure, which is the ratio of seismic shear converted acceleration to yield acceleration.

### 7.1 TATB transcendence intensity magnification calculation method

The seismic shear, acceleration and yield acceleration calculation methods are applicable to multistone masonry structures. Based on the test data and related standards, a transcendence intensity magnification calculation method applicable to multistory masonry

**Table 7** Peak acceleration of the specimens

No.	Displacement peak / mm	Acceleration peak / $m/s^2$	Two floor acceleration ( $m/s^2$ )			Three floor acceleration ( $m/s^2$ )				
			First floor top	Second floor top	Amplification factor	First floor top	Second floor top	Amplification factor	Third floor top	Amplification factor
1	8.340	1.042	1.369	1.507	1.446	1.487	1.509	1.448	1.913	1.836
2	12.180	1.598	1.623	2.195	1.374	1.687	1.816	1.136	2.282	1.428
3	15.890	2.881	3.090	3.540	1.229	2.878	3.343	1.160	4.750	1.649

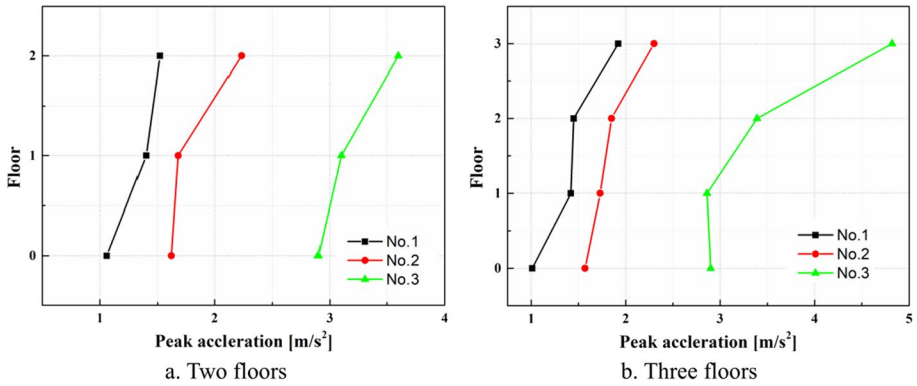


Fig. 30 Acceleration response of the TATB

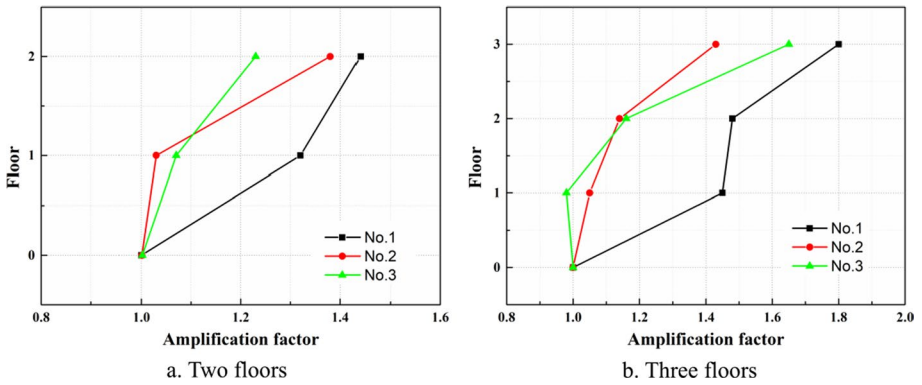


Fig. 31 The variations in the acceleration amplification coefficient

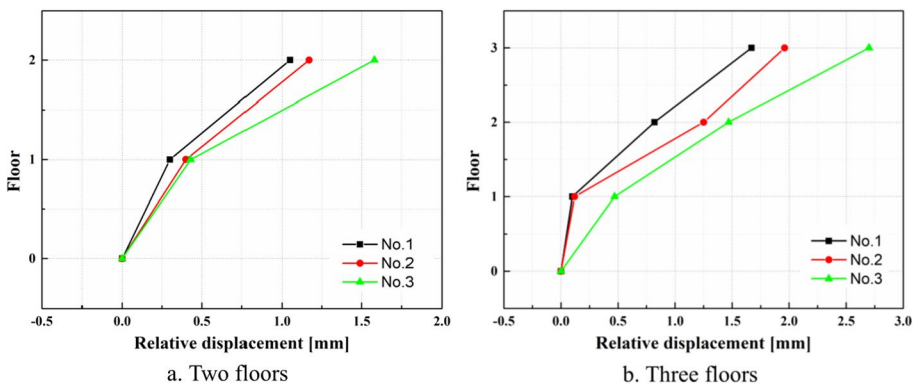


Fig. 32 Displacement response of the TATB

**Table 8** Peak acceleration of the specimens

No.	Two floor displacement (mm)				Three floor displacement (mm)				Relative displacement		
	First floor bottom	First floor top	Relative displacement	Second floor top	First floor bottom	First floor top	Relative displacement	Second floor top		Third floor top	Relative displacement
1	9.16	9.43	0.27	10.21	9.68	9.72	0.04	10.5	11.33	0.82	1.65
2	12.29	12.67	0.38	13.51	12.55	12.62	0.07	13.83	14.53	1.28	1.98
3	16.12	16.53	0.41	17.71	16.22	16.65	0.43	17.66	18.84	1.44	2.62



structures is proposed. The transcendence intensity magnification calculation method for multistory masonry structures is the ratio of seismic shear converted acceleration to yield acceleration.

### 7.1.1 Seismic shear translates to acceleration

According to the bottom shear method, the interlayer seismic shear force of masonry structures is calculated by Eq. (3) (JGJ161-2008, 2008).

$$Q_s = \alpha_{maxb} G_{eq} = k\beta G_{eq} \tag{3}$$

where  $\alpha_{maxb}$  is the maximum horizontal seismic influence coefficient under the action of an earthquake;  $G_{eq}$  is the equivalent total gravity load of the structure;  $k$  is the ratio of the peak seismic acceleration to the gravitational acceleration; and  $\beta$  is the design value of the seismic acceleration amplification coefficient, which is 2.25 (Li et al. 2013).

Yin and Yang (2004) predicted the failure state of masonry structures under earthquakes by the ratio of floor seismic shear to floor shear resistance, which is the excess strength multiplier. The calculation method for exceeding the strength ratio is shown in Eq. (4).

$$E = \frac{Q_s}{V_s} = \frac{\frac{Q_s}{A_s \bar{w}}}{\frac{V_s}{A_s \bar{w}}} = \frac{\alpha_{sE}}{\alpha_{sy}} \tag{4}$$

$$a_{sy} = \frac{\bar{V}_s}{\bar{w}} = \frac{0.325}{A_s d} F_s R_\tau \left( 1 + \sum_1^k C_i \right) = \frac{1}{A_s \cdot 0.012d} 0.66 f_{vE,k} A \left( 1 + \sum_1^k C_i \right) \tag{5}$$

$$R_\tau = 0.8 \sqrt{R_k^2 + 0.5(n - s + 1)R_k} \tag{6}$$

$$f_{vE,k} = 0.07 \sqrt{f_2 + 0.8(n - s + 1)\sqrt{f_2}} \tag{7}$$

where  $E$  exceeds the intensity magnification;  $Q_s$  is the s-floor seismic shear strength;  $V_s$  is the s-floor shear resistance;  $\bar{w}$  is the weight per square meter of floor (component weight and the live load);  $\alpha_{sE}$  is the s-floor seismic shear converted acceleration (g);  $\alpha_{sy}$  is the yield acceleration (g) of the s floor;  $\bar{V}$  is the average shear strength per unit area of floor s;  $F_s$  is the sum of the cross-sectional area of the longitudinal and horizontal brick walls of the S floor without deduction of the opening ( $m^2$ );  $A_s$  is the floor area of the s-floor ( $m^2$ );  $D$  is the floor gravity correction coefficient of the value;  $R_\tau$  is the masonry standard compressive strength ( $N/mm^2$ );  $R_k$  is the standard shear strength of masonry with nonseismic design ( $N/mm^2$ );  $n$  is the number of floors;  $s$  is the number of layers calculated;  $C_i$  is the correction coefficient of fortification standards, seismic measures and other factors;  $f_2$  is the average compressive strength of mortar ( $N/mm^2$ );  $f_{vE,k}$  is the standard value of the seismic shear strength of masonry considering the influence of positive stress;  $A$  is the sum of the cross-sectional area of the longitudinal and transverse walls of the layer without deduction of the opening ( $m^2$ ); and  $A_c$  is total cross-sectional area of floor structural columns ( $m^2$ ).

The equivalent gravity load of the structure is equal to the product of the building area and the calculated weight per square meter of the floor, and the calculation method

for converting the seismic shear force of the masonry structure to the acceleration can be obtained from Eqs. (3) and (4); see Eq. 8.

$$a_{sE} = k\beta \tag{8}$$

### 7.1.2 Yield acceleration

According to JGJ161-2008 (JGJ161-2008, 2008), the ultimate bearing capacity of the wall is calculated via Eq. 10. The average shear strength in Eq. 10 has no shear reserve. The coefficient  $\gamma_{bE}$  is used for correction. The standard value of the shear strength is taken to calculate the excess strength ratio.  $\gamma_{bE}$  is equal to 1. Equation 10 is obtained from Eq. 9.

$$V_{bi} = \gamma_{bE}\zeta_N f_{v,m} A_i \tag{9}$$

$$V_i = \zeta_N f_{v,m} A_i = f_{vE,k} A_i \tag{10}$$

where  $V_{bi}$  is the ultimate seismic shear ultimate bearing capacity of the  $i$ th wall;  $V_i$  is the standard value of the seismic shear bearing capacity of the  $i$ th wall;  $\gamma_{bE}$  is the seismic adjustment coefficient of the ultimate bearing capacity;  $\zeta_N$  is the wall shear strength positive stress influence coefficient;  $f_{v,m}$  is the masonry seismic shear strength average;  $f_{vE,k}$  is the standard value of the seismic shear strength of masonry considering the influence of positive stress; and  $A_i$  is the cross-sectional area of the  $i$ th wall.

Assuming that no matter where the earthquake occurred, there is 60% of the wall resistance to earthquakes. The seismic shear bearing capacity of the structure can be obtained from Eq. (10), as shown in Eq. (11):

$$V_s = 0.6 \sum f_{vE,k} A_i = 0.6 f_{vE,k} A \tag{11}$$

where  $A$  is the total cross-sectional area of the wall ( $m^2$ ) minus the doors and windows.

The yield acceleration can be obtained from Eq. 2 and Eq. 10, as shown in Eq. (12).

$$a_{sy} = \frac{V_s}{A_s \bar{w}} = 0.6 \frac{A f_{vE,k}}{A_s \bar{w}} = 0.6 \lambda \frac{f_{vE,k}}{\bar{w}} \left( 1 + \sum C_i \right) \tag{12}$$

where  $A_s$  is the total area of the building structure and  $\lambda$  is the structure with wall content.

When calculating the yield acceleration, it is necessary to determine the wall inclusion rate, the calculated seismic shear strength of the TATB under the influence of positive stress and the weight of the structure per unit area. The wall inclusion rate is the ratio of the total cross-sectional area of the wall to the building area after deducting the door and window areas. Considering the influence of positive stress, the standard value of the seismic shear strength of a masonry structure ( $f_{vE,k}$ ) is related to the positive stress of the masonry.  $\bar{w}$  is related to the vertical load and the weight of the structure.

When calculating the seismic shear strength of a wall, the influence of positive stress needs to be considered. According to JGJ161-2008 (JGJ161-2008, 2008), the positive stress influence coefficient calculation method for stone block masonry is shown in Eq. (13).

$$\zeta_N = \begin{cases} 1 + \frac{0.25\sigma_0}{f_v} & \left( \frac{\sigma_0}{f_v} \leq 5 \right) \\ 2.25 + 0.17\left(\frac{\sigma_0}{f_v} - 5\right) & \left( \frac{\sigma_0}{f_v} > 5 \right) \end{cases} \tag{13}$$

where  $\sigma_0$  is the positive stress of the masonry (N/mm<sup>2</sup>) and  $f_v$  is the design value of the shear strength of the masonry (N/mm<sup>2</sup>).

The positive stress at half of the wall for a multistory masonry structure is calculated by Eq. (14) (GB50003–2011 2011).

$$\sigma_0 = \frac{(2.18 + 39.9\lambda)A_s h}{A} = \frac{(2.18 + 39.9\lambda)h}{1000\lambda} \tag{14}$$

where h is the height of the wall.

The calculation method of the design value of the shear strength of stone masonry is shown in Eqs. 15 and 16:

$$f_v = \frac{f_{v,k}}{1.6} = \frac{1}{1.6} (1 - 1.645\delta_f)f_{v,m} = 0.028937\sqrt{f_2} \tag{15}$$

$$f_{v,m} = 0.069\sqrt{f_2} \tag{16}$$

where  $f_{v,k}$  is the masonry seismic shear strength standard value and  $\delta_f$  is the coefficient of variation (see Sect. 2).

Equation 14 and Eq. 15 are substituted into Eq. 13. The seismic shear strength of the masonry can be obtained from Eq. 16, giving Eqs. 17, 18, and 19.

$$f_{vE,k} = \zeta_N f_{vk} \tag{17}$$

When  $\sigma_0/f_v \leq 5$ :

$$f_{vE,k} = \zeta_N f_{vk} = 0.046299\sqrt{f_2} + \frac{0.000872}{\lambda} + 0.01596 \tag{18}$$

When  $\sigma_0/f_v > 5$ :

$$f_{vE,k} = \zeta_N f_{vk} = 0.0648\sqrt{f_2} + \frac{0.000593}{\lambda} + 0.01085 \tag{19}$$

The wall content rate needs to satisfy  $\lambda < \frac{2.18}{144.7\sqrt{f_2}-39.9}$  when  $\sigma_0/f_v > 5$ . The compressive strength of the mortar is lower. A larger upper limit of the wall inclusion rate is required to meet  $\sigma_0/f_v > 5$ . For example, when the compressive strength of the mortar is 0.4 MPa, the wall content rate is 4.2%. The higher the compressive strength of the mortar is, the lower the required wall content. However, such a low wall content rate is obviously inconsistent with reality. Therefore, the seismic shear strength of the TATB can be calculated by Eq. 14.

Substituting the calculated weight per unit area of the structure and Eq. 17 into Eq. 11, the equation (Eq. 20) yield acceleration of the TATB is obtained.

$$a_{sy} = \frac{27.78\lambda\sqrt{f_2} + 9.58\lambda + 0.5232}{2.18 + 71.4\lambda} \left( 1 + \sum C_i \right) \tag{20}$$

## 7.2 Assessment of the seismic resistance of TATBs

### 7.2.1 Earthquake establishment commutation acceleration

The converted seismic shear acceleration corresponding to different seismic accelerations (Table 9) can be obtained from Eq. 8.

Compared with the experimental results, the calculated converted seismic shear acceleration is significantly greater than the reaction acceleration of the structure from the shaking table test. Therefore, it is necessary to correct the design of the seismic acceleration amplification coefficient. When the design value of the seismic acceleration amplification factor is 0.74, the converted seismic shear acceleration is similar to the test results (Table 10).

### 7.2.2 Results of yield acceleration

Equation (20) shows that the yield acceleration of the structure is affected by the mortar strength, wall content rate and correction coefficient. The correction coefficient  $C_i$  includes structural measures, fortification standards and other factors, and its determination requires a large number of seismic damage investigations and calculation case analyses; moreover, its influence is not considered when calculating the yield acceleration here. The yield acceleration calculation results of the buildings without considering the correction factor are shown in Table 11. The mortar compressive strength and stone compressive strength were derived from the material tests in Sect. 3.

### 7.2.3 Results of the structural overstrength multiplier

According to Table 9 and Table 10, the structural overstrength multiplier under different seismic intensities can be obtained from Eq. (2), as shown in Table 12.

**Table 9** Converted seismic shear acceleration

Peak ground shaking	0.1042 g	0.1598 g	0.2881 g
The converted seismic shear acceleration	0.2345 g	0.3596 g	0.6482 g

**Table 10** Converted seismic shear acceleration

Peak ground shaking	0.1042 g	0.1598 g	0.2881 g
Ground shaking response acceleration	0.1913 g	0.2282 g	0.4750 g
The converted seismic shear acceleration	0.1737 g	0.2664 g	0.4802 g

**Table 11** Yield acceleration

Compression of the mortar/MPa	Compression of the stone/MPa	Yield acceleration/g
0.408	67.92	0.32

### 7.2.4 Assessment of structural damage

The relationship between the seismic damage level of the TATB and the  $E$  value of the intensity exceeding ratio is shown in Table 13 (GB/T 18208.3-2000, 2000; Yao et al. 2022). Based on Tables 11 and 12, the failure states of the structure under seismic action of different intensities were obtained, as shown in Table 14.

Table 14 shows that the TATB is basically intact and slightly damaged when the ground motion peak acceleration is  $1.021 \text{ m/s}^2$ . The TATB is moderately damaged when the ground motion peak acceleration is equal to  $1.566 \text{ m/s}^2$ . When the peak acceleration of ground motion is  $2.824 \text{ m/s}^2$ , the TATB is seriously damaged or destroyed. The shaking table test results are used as a reference, and the results are compared with the calculation results. The scale model is constructed according to a certain scale on the basis of the size of the original structure. However, the scale model can reflect the reaction of the original structure under seismic action. However, it inevitably has a certain difference from the original structure reaction. The acceleration similarity coefficient in the test similarity relationship is 1.0. The acceleration response of the architectural model is the acceleration response of the TATB. The failure state of the TATB model under different intensities of seismic action is equal to the failure state of the actual structure.

The calculation results of the seismic failure state of the TATB are the same as the test results when the peak acceleration of ground motion is  $1.042 \text{ m/s}^2$ . When the peak acceleration of ground motion is  $1.598 \text{ m/s}^2$  and  $2.881 \text{ m/s}^2$ , the calculated structural failure state is more severe than the test results. The test model is the scaled model.

There are some errors in deriving the seismic performance of the prototype structure from the experimental results of the 1/5-scale model. Comparing the seismic performance of a TATB in a shaking table test and the damage state of a TATB under an earthquake, the damage state of the actual structural situation is greater than that of

**Table 12** Structural overstrength multiplier

Compression of the mortar/MPa	Ground Shaking Response Acceleration		
	0.1042 g	0.1598 g	0.2881 g
0.408	0.73	1.12	2.03

**Table 13** Correspondence between the value of the beyond strength multiplier  $E$  and the damage state of the structure

Damage state	Basically intact	Slightly damaged	Moderately damaged	Seriously damaged	Destroyed
TATB	$E \leq 1$	$1.0 < E \leq 1.3$	$1.3 < E \leq 1.7$	$1.7 < E \leq 2.0$	$2.0 < E$

**Table 14** Expected damage states of TATBs

Compression of the mortar/MPa	Ground shaking response acceleration		
	0.1042 g	0.1598 g	0.2881 g
0.408	Slightly damaged	Moderately damaged	Seriously damaged

the test model under ground shaking. Therefore, this paper believes that the calculation results are close to the actual situation.

## 8 Conclusion

The parameters for calculating the seismic performance of TATBs are obtained via mechanical property tests of the construction materials and compressive strength and shear strength tests of the walls. According to the transcendence intensity magnification calculation method, the calculation method of the transcendence intensity rate applicable to TATBs is derived with reference to the code of China. The seismic resistance of TATBs is evaluated by this method and compared with the test results.

The damage to the TATB wall in the compression test showed irregular penetrating cracks in the longitudinal sides of the wall. A large area of stone fell off at the bottom of the side of the wall. The uneven distribution of the mass and stiffness of the stone masonry wall resulted in a jagged load–displacement curve. The wall maintained a period of ductility after the compressive strength of the TATB wall reached the elastic extreme. The TATB walls were sheared with diagonal penetrating cracks in the quasistatic test, accompanied by a large number of vertical and transverse cracks. As the displacement increased, the rate of degradation of the stiffness of the wall gradually decreased. The specimen stiffness reached a minimum value when the specimen was subjected to ultimate loads.

The flat elevation geometric irregularity of the TATB was particularly evident on the 2nd and 3rd floors. A change in the stiffness and bearing capacity resulted in a “V” shear slant crack. The irregularity of the plane and façade led to asymmetric torsion of the TATB. The asymmetric torsion resulted in a difference of approximately 10% between the peak acceleration and the peak displacement on the same floor. The presence of the torsional effect seriously affected the seismic performance of the structure.

When the peak acceleration of ground motion was  $1.021 \text{ m/s}^2$ ,  $1.566 \text{ m/s}^2$  and  $2.824 \text{ m/s}^2$ , the TATB had slight damage, moderate damage, and severe damage, respectively. By correcting the seismic acceleration amplification coefficient, the failure state of the TATB in the shaking table test was found to be consistent with the damage state calculated to exceed the intensity assessment. The seismic vulnerability of the TATB could be evaluated by transcendence magnification calculation formulas.

This study provides technical data for the seismic performance of TATBs, which has positive significance for the protection of TATBs. However, the structural overstrength multiplier uncorrected with the seismic acceleration amplification factor is greater than the values calculated from the test data. It is possible that the scaled model tends to underestimate the damage to the TATB. Therefore, further experimental or numerical analysis of TATBs is necessary to avoid errors.

**Acknowledgements** This work was financially support by National Natural Science Foundation of China (52178461, 51878124). In addition, Liaoning Provincial Natural Science Fund Guidance Plan (20180550073, 2015020620) by those funding of scientific research projects is gratefully acknowledged.

**Funding** Funding was provided by National Natural Science Foundation of China (Grant no: 52178461, 51878124), Natural Science Foundation of Liaoning Province (Grant no: 20180550073, 2015020620).

## Declarations

**Conflict of interest** We declare that we have no financial and personal relationships with other people or organizations that can inappropriately influence our work. There is no professional or other personal interest of

any nature or kind in any product, service and/or company that could be construed as influencing the position presented in, or the review of, the manuscript entitled. The authors report no conflicts of interest. The authors alone are responsible for the content and writing of this article.

## References

- Ali Q, Ahmad N, Ashraf M, Rashid M, Schacher T (2017) Shake table tests on single-story Dhajji Dewari traditional buildings. *Int J Archit Herit*. <https://doi.org/10.1080/15583058.2017.1338789>
- Ali Q, Ahmad N, Ashraf M, Schacher T (2021) Seismic performance evaluation of two-story Dhajji-Dewari traditional structure. *Int J Archit Herit* 16(8):1233–1251
- Almeida C, Guedes JP, Arêde A, Costa CQ, Costa A (2012) Physical characterization and compression tests of one leaf stone masonry walls. *Constr Build Mater* 30:188–197
- Borri A, Corradi M, Castori G, De Maria A (2015) A method for the analysis and classification of historic masonry. *Bull Earthq Eng* 13(9):2647–2665
- Boscato G, Reccia E, Cecchi A (2018) Non-destructive experimentation: dynamic identification of multi-leaf masonry walls damaged and consolidated. *Compos B Eng* 133:145–165. <https://doi.org/10.1016/j.compositesb.2017.08.022>
- Brando G, De Matteis G, Spacone E (2017a) Predictive model for the seismic vulnerability assessment of small historic centres: application to the inner Abruzzi Region in Italy. *Eng Struct* 153:81–96. <https://doi.org/10.1016/j.engstruct.2017.10.013>
- Brando G, Rapone D, Spacone E, O'Banion MS, Olsen MJ, Barbosa AR, Faggella M, Gigliotti R, Liberatore D, Russo S, Sorrentino L, Bose S, Stravidis A (2017b) Damage reconnaissance of unreinforced masonry bearing wall buildings after the 2015 Nepal, Nepal, Earthquake. *Earthq Spectra* 33(1\_suppl):243–273. <https://doi.org/10.1193/010817eqs009m>
- Candeias PX, Campos Costa A, Mendes N, Costa AA, Lourenço PB (2017) Experimental assessment of the out-of-plane performance of masonry buildings through shaking table tests. *Int J Archit Herit* 11(1):31–58
- Carocci CF (2012) Small centres damaged by 2009 L'Aquila earthquake: on site analyses of historical masonry aggregates. *Bull Earthq Eng* 10(1):45–71
- Casolo S, Milani G (2013) Simplified out-of-plane modelling of three-leaf masonry walls accounting for the material texture. *Constr Build Mater* 40:330–351. <https://doi.org/10.1016/j.conbuildmat.2012.09.090>
- Chávez M, Meli R (2013) Shaking table tests of a typical mexican colonial temple: evaluation of two retrofitting techniques. *Earthq Spectra* 29(4):1209–1231
- Chen H, Xie Q, Li Z, Xue W, Liu K (2016) Seismic damage to structures in the 2015 nepal earthquake sequences. *J Earthquake Eng* 21(4):551–578. <https://doi.org/10.1080/13632469.2016.1185055>
- Chen XZ, Sun BT, Yan PL (2017) A brief analysis of hazard distribution characteristics and structural damage of the 63 magnitude Kangding earthquake in Sichuan. *Earthq Eng Vib* 37(02):1–9
- Corradi M, Borri A (2018) A database of the structural behavior of masonry in shear. *Bull Earthq Eng* 16(9):3905–3930
- Costa AA, Arêde A, Campos Costa A, Penna A, Costa A (2013a) Out-of-plane behaviour of a full-scale stone masonry façade. Part 1: specimen and ground motion selection. *Earthq Eng Struct Dyn* 42:2081–2095. <https://doi.org/10.1002/eqe.2313>
- Costa AA, Arêde A, Costa AC, Penna A, Costa A (2013b) Out-of-plane behaviour of a full scale stone masonry façade. Part 2: shaking table tests. *Earthq Eng Struct Dyn* 42:2097–2111
- D'Amato M, Sullà R (2021a) Investigations of masonry churches seismic performance with numerical models: application to a case study. *Arch Civ Mech Eng*. <https://doi.org/10.1007/s43452-021-00312-5>
- D'Amato M, Luchin G, De Matteis G (2023) A preliminary study on properties of a weak units-strong mortar masonry: the case study of Matera Tufo masonry (Italy). *Int J Archit Herit* 17(7):1115–1136. <https://doi.org/10.1080/15583058.2021.2015641>
- D'Ayala DF, Paganoni S (2011) Assessment and analysis of damage in L'Aquila historic city centre after 6th April 2009. *Bull Earthq Eng* 9(1):81–104
- de Carvalho Bello CB, Boscato G, Meroi E, Cecchi A (2020) Non-linear continuous model for three leaf masonry walls. *Construct Build Mater* 244:118356. <https://doi.org/10.1016/j.conbuildmat.2020.118356>
- Di Michele F, Spacone E, Camata G, Brando G, Sextos A, Crewe A, Mylonakis G, Diez M, Dihoru L, Varum H (2023) Shaking table test and numerical analyses of a full scale three-leaf masonry wall. *Bull Earthq Eng* 21(10):5041–5081. <https://doi.org/10.1007/s10518-023-01705-y>

- Dimitris P, Konstantinos I, Anna K (2018) Shaking table tests on a stone masonry building: modeling and identification of dynamic properties including soil-foundation-structure interaction. *Int J Archit Herit* 12(6):1019–1037
- Elmenshawi A, Shrive N (2014) Assessment of Multi-Wythe stone masonry subjected to seismic hazards. *J Earthquake Eng* 19(1):85–106
- Felice G, Liberatore D, De Santis S, Gobbin F, Roselli I, Sangirardi M, Sorrentino L (2022) Seismic behaviour of rubble masonry: shake table test and numerical modelling. *Earthq Eng Struct Dyn* 51(5):1245–1266
- Ferreira TM, Costa AA, Arêde A et al (2015) Experimental characterization of the out-of-plane performance of regular stone masonry walls, including test setups and axial load influence. *Bull Earthq Eng* 13:2667–2692
- Fuentes DD, Baquedano Julià PA, D'Amato M, Laterza M (2019) Preliminary seismic damage assessment of mexican churches after september 2017 earthquakes. *Int J Archit Herit* 15(4):505–525. <https://doi.org/10.1080/15583058.2019.1628323>
- Galetzka J et al (2015) Slip pulse and resonance of the Kathmandu basin during the 2015 Gorkha earthquake, Nepal. *Science* 349(6252):1091–1095. <https://doi.org/10.1126/science.aac6383>
- Gautam D (2017) Seismic performance of world heritage sites in Kathmandu Valley during Gorkha Seismic sequence of April–May 2015. *J Perform Construct Facil*. [https://doi.org/10.1061/\(ASCE\)CF.1943-5509.0001040](https://doi.org/10.1061/(ASCE)CF.1943-5509.0001040)
- GB50003–2011 (2011) Code for design of masonry structure. China Architecture & Building Press. 2011. (In Chinese)
- GB 5009–2011 (2011) Load code for the design of building structures. Beijing, China: MOHURD; 2012. (in Chinese)
- GB 50011–2010 (2010) Code for seismic design of buildings. Beijing, China Architecture & Building Press. 2010 (In Chinese)
- GB/T 18208.3–2000 (2000) Earthquake fieldwork part III: investigation specifications. Beijing, State Bureau of Quality and Technical Supervision
- GB/T2542–2012 (2012) Test method for wall bricks. Standardization Administration of China (SAC). Beijing, 2012. (in Chinese)
- GB/T50129–2011 (2011) Standard for test method of basic properties mechanics of masonry. Beijing, China: Ministry of Housing and Urban-Rural Development of the People's Republic of China. (In Chinese)
- Giaretton M, Valluzzi MR, Mazzon N, Modena C (2017) Out-of-plane shake-table tests of strengthened multi-leaf stone masonry walls. *Bull Earthq Eng* 15(10):4299–4317
- Godio M, Vanin F, Zhang S, Beyer K (2019) Quasi-static shear-compression tests on stone masonry walls with plaster: Influence of load history and axial load ratio. *Eng Struct* 192:264–278
- Guerrini G, Senaldi I, Graziotti F, Magenes G, Beyer K, Penna A (2019) Shake-table test of a strengthened stone masonry building aggregate with flexible diaphragms. *Int J Archit Herit* 13(7):1078–1097
- Hendry AW, Khalaf FM (2001) Masonry wall construction. Spon Press, London
- Hu RR, Liu JP (2009) Study on the problems in the evolution of vernacular houses in the agricultural areas of Tibet. *J xi'an Univ Archit Technol Nat Sci Edition* 41(03):380–384
- JGJ/T 101–2015 (2015) Specification for seismic test of buildings (in Chinese). Beijing, China: MOHURD; 2015. (In Chinese)
- JGJ161–2008 (2008) Seismic technical specification for building construction in town and village. Beijing, China: Ministry of Housing and Urban-Rural Development of the People's Republic of China. (In Chinese)
- Jiang YH, Yang N, Chang P (2022) Experimental assessment of in-plane behavior of traditional Tibetan three-leaf walls. *Structures* 44(2022):698–712
- Kaushik HB, Rai DC, Jain SK (2007) Stress-strain characteristics of clay brick masonry under uniaxial compression. *J Mater Civ Eng* 19(9):728–739. [https://doi.org/10.1061/\(ASCE\)0899-1561\(2007\)19:9\(728\)](https://doi.org/10.1061/(ASCE)0899-1561(2007)19:9(728))
- Krzan M, Gostic S, Cattari S, Bosiljkov V (2015) Acquiring reference parameters of masonry for the structural performance analysis of historical buildings. *Bull Earthq Eng* 13(1):203–236
- Lagomarsino S, Resemini S (2009) The assessment of damage limitation state in the seismic analysis of monumental buildings. *Earthq Spectra* 25(2):323–346
- Lagomarsino S, Penna A, Galasco A, Cattari S (2013) TREMURI program: an equivalent frame model for the nonlinear seismic analysis of masonry buildings. *Eng Struct* 56:1787–1799
- Li GQ, Li J, Su XZ (2013) Seismic design of building structures. China Construction Industry Press, Beijing
- Li P, Liu YC, Zhou K et al (2020) A review of similar design for shaker modeling tests. *J Disaster Prev Sci Technol Inst* 22(04):29–35



- Li C, Chen B, Sennah K, Liu JP, Liao MX (2023) Experimental study on axial compressive behavior of stone masonry with ultra-high performance mortar. *Mater Struct* 56:124
- Liang B, Hou J, He Z (2023a) Rapid assessment method to assess vulnerability of structures using vulnerability index and disaster matrix. *Bull Earthq Eng* 21:2691–2722
- Liang B, Zhang H, Liu Z, Hou J (2023b) The influence of different types of mortar on the compressive strength of masonry. *J Build Eng* 65:105635. <https://doi.org/10.1016/j.jobe.2022.105635>
- Lombillo I, Thomas C, Villegas L, Fernández-Álvarez JP, Norambuena-Contreras J (2013) Mechanical characterization of rubble stone masonry walls using non and minor destructive tests. *Constr Build Mater* 43:266–277
- Lou YF, Sun BT (2014) An earthquake damage prediction method for brick masonry structures considering the effect of structural columns. *J Civ Eng* 47(8):42–46
- Mazzon N, Chavez CM, Valluzzi MR, Casarin F, Modena C (2010a) Shaking table tests on multi-leaf stone masonry structures: analysis of stiffness decay. *Adv Mater Res* 133–134:647–652
- Mazzon N, Chavez CM, Valluzzi MR, Casarin F, Modena C (2010b) Shaking table tests on multi-leaf stone masonry structures: analysis of stiffness decay. *Adv Mater Res* 133–134:647–652. <https://doi.org/10.4028/www.scientific.net/AMR.133-134.647>
- Miccoli L, Müller U, Pospíšil S (2017) Rammed earth walls strengthened with polyester fabric strips: experimental analysis under in-plane cyclic loading. *Constr Build Mater* 149:29–36
- Rafi MM, Lodi SH, Kumar A, Verjee F (2019) Seismic risk reduction in northern Pakistan. *Proc Inst Civ Eng Munic Eng* 172(3):185–194
- Ravula MB, Subramaniam KVL (2019) Cohesive-frictional interface fracture behavior in soft-brick masonry: experimental investigation and theoretical development. *Mater Struct*. <https://doi.org/10.1617/s11527-019-1333-1>
- Rovero L, Alecci V, Mechelli J, Tonietti U, De Stefano M (2016) Masonry walls with irregular texture of L'Aquila (Italy) seismic area: validation of a method for the evaluation of masonry quality. *Mater Struct* 49(6):2297–2314
- Schiavi A, Cellai G, Secchi S, Brocchi F, Grazzini A, Prato A, Mazzoleni F (2019) Stone masonry buildings: analysis of structural acoustic and energy performance within the seismic safety criteria. *Constr Build Mater* 220:29–42
- Senaldi I, Magenes G, Penna A, Galasco A, Rota M (2013) The effect of stiffened floor and roof diaphragms on the experimental seismic response of a full-scale unreinforced stone masonry building. *J Earthquake Eng* 18(3):407–443
- Senaldi IE, Guerrini G, Comini P, Graziotti F, Penna A, Beyer K, Magenes G (2019) Experimental seismic performance of a half-scale stone masonry building aggregate. *Bull Earthq Eng* 18(2):609–643
- Siegesmund S, Sneathlage R (2011) *Stone in architecture: properties, durability*. Springer, Berlin
- Silva B, Dalla Benetta M, da Porto F, Modena C (2014) Experimental assessment of in-plane behaviour of three-leaf stone masonry walls. *Construct Build Mater* 53:149–161. <https://doi.org/10.1016/j.conbuildmat.2013.11.084>
- Silva BQ, Pappas A, Guedes JM, da Porto F, Modena C (2016) Numerical analysis of the in-plane behaviour of three-leaf stone masonry panels consolidated with grout injection. *Bull Earthq Eng* 15(1):357–383. <https://doi.org/10.1007/s10518-016-9969-5>
- JGJ/T98–2010 (2010) Specification for mix proportion design of masonry mortar. Beijing, China: Ministry of Housing and Urban-Rural Development of the People's Republic of China. (in Chinese)
- JGJ/T70–2009 (2009) Standard for test method of performance on building mortar (in Chinese). Beijing, China: MOHURD; 2009. (In Chinese)
- Vintzileou E, Mouzakis C, Adami CE, Karapitta L (2015) Seismic behavior of three-leaf stone masonry buildings before and after interventions: shaking table tests on a two-storey masonry model. *Bull Earthq Eng* 13(10):3107–3133
- Wang BW, Li XG (2010) Study on the similarity relationship of shaking table test models by neglecting the effect of gravity. *Shanxi Construct* 36(21):77–78
- Wang Y, Liu AW, Li XX, Wang XH (2021) Vulnerability analysis of typical residential buildings in Tibet based on earthquake damage data. *Earthq Def Technol* 16(02):245–252
- World Heritage List (2023) Historic Ensemble of the Potala Palace, Lhasa. <https://whc.unesco.org/en/list/>
- Xu H, Du NN, Yu ZX, Qiao YK (2019) Seismic collapse resistance of Qiang stone masonry residential buildings in Sichuan, Tibet and China. *J Southwest Jiaotong Univ* 54(05):1021–1029
- Xu XS, Chi-La MY (2009) Research on seismic-resistant technology of qiang traditional architecture and its inheritance. *Journal of southwest university for nationalities (humanities and social sciences edition)*, 30(02):11–14
- Xue J, Ling H, Zhao X, Zhang F, Zhou H (2022) Seismic performance on stone masonry loess cave retro-fitted using composite materials. *J Build Eng* 46:103704. <https://doi.org/10.1016/j.jobe.2021.103704>

- Yang N, Teng DY (2020) Shear performance of Tibetan stone masonry under shear-compression loading. *Eng Mech* 37(2):221–229
- Yao X, Liang B, Sun B, Wang D, Gao W (2022) Integrated disaster matrix and vulnerability index analyze the seismic performance of typical structures in rural villages in historical earthquakes. *Adv Struct Eng* 25(14):2981–2997
- Yin ZQ, Yang SW (2004) Earthquake loss analysis and defense standards. Earthquake Press, Beijing
- Zhang S, Taheri Mousavi SM, Richart N, Molinari J-F, Beyer K (2017) Micro-mechanical finite element modeling of diagonal compression test for historical stone masonry structure. *Int J Solids Struct* 112:122–132
- Zhao X, Xue J, Zhang F (2022) Experimental seismic performance of a reduce-scale stone masonry loess cave with traditional buildings. *Bull Earthq Eng* 20(10):5233–5267. <https://doi.org/10.1007/s10518-022-01380-5>
- Zhu F, Wang FL, Sun XJ, Zhao Y (2012) Shaking table test on unreinforced stone masonry pagoda. *Appl Mech Mater* 166–169:730–733

**Publisher's Note** Springer Nature remains neutral with regard to jurisdictional claims in published maps and institutional affiliations.

Springer Nature or its licensor (e.g. a society or other partner) holds exclusive rights to this article under a publishing agreement with the author(s) or other rightsholder(s); author self-archiving of the accepted manuscript version of this article is solely governed by the terms of such publishing agreement and applicable law.